

Constraints from Fermi observations of Long Gamma-Ray Bursts on cosmological parameters

Huifeng Wang,¹ Nan Liang,^{1,2,3*}

¹Key Laboratory of Information and Computing Science Guizhou Province, Guizhou Normal University, Guiyang, Guizhou 550025, China

²School of Cyber Science and Technology, Guizhou Normal University, Guiyang, Guizhou 550025, China

³Joint Center for FAST Sciences Guizhou Normal University Node, Guiyang, Guizhou 550025, China

Accepted XXX. Received YYY; in original form ZZZ

ABSTRACT

In this paper, we compile a *Fermi* sample of the *long* GRB observations from 15 years of GBM catalogue with identified redshift, in which the GOLD sample contains 123 long GRBs at $z \leq 5.6$ and the FULL sample contains 151 long GRBs with redshifts at $z \leq 8.2$. The Amati relation (the $E_{p,i}$ - E_{iso} correlation) are calibrated at $z < 1.4$ by a Gaussian Process from the latest observational Hubble data (OHD) with the cosmic chronometers method so that GRBs at high-redshift $z \geq 1.4$ can be used to constrain cosmological models via the Markov chain Monte Carlo (MCMC) method. From the cosmology-independent GRBs with the GOLD sample at $z \geq 1.4$ and the Pantheon+ sample of type Ia supernovae (SNe Ia) at $0.01 < z \leq 2.3$, we obtain $\Omega_m = 0.354 \pm 0.018$, $H_0 = 73.05 \pm 0.2$ km/s/Mpc for the flat Λ CDM model; $w_0 = -1.22^{+0.18}_{-0.15}$ for the flat w CDM model; and $w_a = -1.12^{+0.45}_{-0.83}$ for the flat Chevallier-Polarski-Linder model at the 1σ confidence level. Our results with the GOLD and FULL sample are almost identical, which are more stringent than the previous results with GRBs.

Key words: gamma-rays: general < Resolved and unresolved sources as a function of wavelength, cosmology: observations < Cosmology

1 INTRODUCTION

Gamma-ray bursts (GRBs) are the most intense explosions observed to occur in the high redshift range measured up to $z = 8 \sim 10$, e.g., GRB 090423 at $z = 8.2$ (Tanvir et al. 2009; Salvaterra et al. 2009), and GRB 090429 at $z = 9.4$ (Cucchiara et al. 2011), which can be used to probe the universe beyond the type Ia supernovae (SNe Ia) observed at the maximum redshift about $z \sim 2$. Recently, several luminosity (or energy) relations of GRBs between measurable spectroscopic properties that can be related to an intrinsic burst physical property and their luminosity or energy have been proposed, e.g. the prompt emission correlations (Norris, Marani, & Bonnell 2000; Fenimore & Ramirez-Ruiz 2000; Amati et al. 2002; Schaefer 2003; Yonetoku et al. 2004; Ghirlanda et al. 2004), and prompt-afterglow emission correlations (Liang & Zhang 2005; Dainotti et al. 2008, 2011, 2017; Dainotti & Del Vecchio 2017; Dainotti & Amati 2018; Bernardini et al. 2012; Izzo et al. 2015; Tang et al. 2019). Therefore, GRBs can be used as standard candles to probe cosmology at high redshift range e.g., Dai et al. (2004); Liang & Zhang (2006); Wang & Dai (2006); Ghirlanda et al. (2006); Schaefer (2007) and Amati & Della Valle. (2013). See Luongo & Muccino (2021a) for reviews.

In order to avoid the circularity problem (Ghirlanda et

al. 2006), the simultaneous method (Amati et al. 2008) in which the parameters of the relationship and the cosmological model fitting simultaneously has also been proposed. Liang et al. (2008) proposed a cosmological model-independent method to calibrate GRBs relations at low redshift from SNe Ia without any cosmological assumption. Therefore, the GRB Hubble diagram at high redshift can be used to constrain cosmological models (Wei & Zhang 2009; Wei 2010; Liang et al. 2010, 2011; Liu & Wei 2015). On the other hand, Amati et al. (2019) proposed an alternative method to calibrate the GRB relation of 193 GRBs by using the observational Hubble data (OHD) obtained with the cosmic chronometers (CC) method (Montiel et al. 2021; Luongo & Muccino 2021b, 2023).

The so-called Amati relation (Amati et al. 2002), which connects the spectral peak energy (E_p) and the isotropic equivalent radiated energy (E_{iso}) has been widely used to estimate cosmological parameters (Amati et al. 2006, 2008, 2009; Amati & Della Valle. 2013; Amati et al. 2019; Wei 2010; Wang et al. 2016; Demianski et al. 2017a,b; Lusso et al. 2019). Quantified by the T_{90} parameter (the time interval over which 90% of the gamma-ray emission is measured) with a division at 2s by the gamma-ray duration, GRBs can be classified into the *short* GRBs (SGRBs) and the *long* GRBs (LGRBs), which are mostly associated to the merger of compact objects (Type I) and associated to the collapse of certain types of massive stars (Type II), respectively. Previous analyses of the $E_p - E_{iso}$ plane of GRBs shows that different classes of

* E-mail:liangn@bnu.edu.cn

GRBs exhibit different behaviours: while normal long GRBs follow the $E_p - E_{\text{iso}}$ correlation, short GRBs do not (e.g., Amati et al. (2006)).

On a mission to study the universe at high energies, the *Fermi* Gamma-ray Space Telescope was launched on 2008 June, including two main instruments: the Gamma-ray Burst Monitor (GBM) and the Large Area Telescope (LAT) with unprecedented sensitivity to gamma-rays overlapping the GBM energy range and extending it up to 300 GeV (Von Kienlin et al. 2020) which provides a powerful tool for studying GRBs. Recently, Amati et al. (2009) found that *Fermi* GRBs are fully consistent with the Amati relation, based on *Fermi*/GBM and LAT spectral measurements (with a cutoff at GRB090424); Wei (2010) used the cosmology-independent method (Liang et al. 2008) to calibrate the Amati relation with 109 GRBs, including 14 additional GRBs (with a cutoff at GRB091208B detected by *Fermi*); Wang et al. (2016) standardized the Amati relation by the cosmology-independent calibration method and the simultaneous method with 151 GRB data, including further 42 GRBs (with a cutoff at GRB140213A detected by *Fermi*). Dirirsa et al. (2019) found that the Amati relation is satisfied by the 25 long GRBs with *Fermi*-LAT sample (from June 2008 to September 2017) detected simultaneously by *Fermi* GBM and LAT, together with a sample of 94 GRBs selected from Wang et al. (2016), which are not in *Fermi* sample or counted twice; Khadka et al. (2021) compiled a total 220 GRB sample (the A220 sample) in which a data set of 118 GRBs (the A118 sample)¹ with the smallest intrinsic dispersion is suitable for constraining cosmological parameters.

More recently, Montiel et al. (2021) obtained a refined set of 74 *long* GRBs from a total 107 data of *Fermi*-GBM catalogue (from August 2008 to March 2019) at $0.117 \leq z \leq 5.283$ based on criteria such as redshift and spectral signal-to-noise ratio, to calibrate the Amati relation through a Bezier parametric curve fitted from the OHD at $z \leq 1.43$. Jia et al. (2022) tested the Amati relation by using 221 GRBs (the J221 sample) which is based on the previous data from Wang et al. (2016); Amati et al. (2019) that appear in both *Swift* and *Fermi* catalogs, and 49 GRBs from *Fermi* catalog (from 2013 to March 2021). Dainotti et al. (2023) compiled a total sample of 86 GRBs with the relationship between the spectral and temporal indices using closure relation from the GRBs that have been fitted in the *Fermi*-LAT Second GRB Catalog (2FLGC) with 186 GRBs observed from 2008 to 2018.

With the enhancement of the number of GRBs with measured redshift and spectral parameters, Liang et al. (2022) used a Gaussian Process to calibrate the A219 sample² from the Pantheon sample (Scolnic et al. 2018) which contains 1048 SNe and constrained Dark Energy models with GRBs at high redshift. Li, Zhang & Liang (2023) calibrated GRBs from the latest 32 OHD using Gaussian Process to construct the GRB Hubble diagram. Xie et al. (2023) calibrated the J221 sample with the Amati relation by the Gaussian Process from the Pantheon+ sample (Scolnic et al. 2022) which contains 1701 SNe light curves of 1550 spectroscopically confirmed

SNe Ia. Zhang et al. (2023) calibrated the Amati relation by the machine learning methods for reconstructing distance-redshift relation from the Pantheon+ sample. Wang et al. (2024) constrain the emergent dark energy models with the cosmology-independent GRBs at high-redshift and OHD to find a large value of H_0 which is close to the results of local measurement from the *Supernova H_0 for the Equation of State* (SH0ES) Collaboration (Riess et al. 2022).

In this paper, we present a sample of long GRBs from 15 years of the *Fermi*-GBM catalogue with redshift measured at $0.0785 \leq z \leq 8.2$. The calibration is performed following the recent work (Li, Zhang & Liang 2023) with a compilation of OHD without assuming an a priori cosmological model. Our sample originates from a single catalogue, which are carefully selected to avoid large errors in the determination of luminosity parameters of the Amati relation, thus avoiding selection biases and other instrument-associated systematics. We calibrate the Amati relation with the *Fermi*-GBM catalogue at low-redshift from the latest OHD with the cosmic chronometers method by using a Gaussian Process to obtained GRBs at high-redshift, which can be used to constrain cosmological models in cosmology-independent way.

The paper is organized as follows. In Sec. 2, we present in detail our *Fermi*-GBM LGRBs sample. In Sec. 3, we reconstruct OHD using GaPP and calibrate the Amati relation. In Sec. 4, we present the datasets included in our suite of observations to fit parameters of DE models. We discuss our results and draw conclusion in Sec. 5.

2 DATA SAMPLE

The GBM onboard the *Fermi* Gamma-ray Space Telescope is made up of 12 sodium iodide (NaI) detectors that cover the energy range 8 keV to ~ 1 MeV, and two bismuth germanate oxide (BGO) detectors (b0 and b1) sensitive from 200 keV to 40 MeV. The axes of the NaI detectors in four groups of three on the corners of the spacecraft are oriented to optimize all-sky coverage and enable the localization of GRBs by comparing the relative observed source rates in each detector. The BGO detectors are located on opposite sides of the spacecraft to enable an all-sky view (Meegan et al. 2009). The onboard GBM trigger system for detecting GRBs was first enabled on 2008 July 12 (Paciesas et al. 2012).

The *Fermi*-GBM science team releases GRB catalogs on a regular basis that list the main characteristics of triggered bursts, compiling the data of several completed mission years, including the first catalog: the first two years (Paciesas et al. 2012), second: the four years (Von Kienlin et al. 2014), third: the six years (Bhat et al. 2016), and four: the 10 years (Von Kienlin et al. 2020). The spectral catalogs were accompanied by Goldstein et al. (2012) and Gruber et al. (2014) for the first two and four mission years. Poolakkil et al. (2021) have updated the 10 year spectral catalog (from June 2008 to March 2018) including 122 long GRBs with redshift. Montiel et al. (2021) obtained a refined set of 74 *long* GRBs from a total 107 data of *Fermi*-GBM catalogue (from August 2008 to March 2019) at $0.117 \leq z \leq 5.283$.

In this work, we collect 15 years (2008-2023) of GRB data observed by *Fermi*-GBM with redshift measured. All the

¹ A short GRB090510 discarded from the 119 GRBs (Dirirsa et al. 2019; Khadka & Ratra 2020).

² Removed GRB051109A, which are counted twice in the A220 sample (Khadka et al. 2021). For details, see Liang et al. (2022).

GRB data are obtained from the FERMIGBRST Catalog³, hosted on NASA High Energy Astrophysics Science Archive Research Center (HEASARC), which contains all GBM triggered events classified as GRBs. For the case of GRBs which present no value for the spectral parameters after 2018 June, we use the preliminary spectral analysis results with best fit by a BAND function⁴ for 19 GRBs⁵ reported in GCN (The Gamma-ray Coordination Network) Circulars Archive⁶. For the GRBs of the preliminary spectral analysis results with best fit NOT a BAND function, we download the GBM Burst Data from FTP archive⁷ to calculate parameters with best fit by BAND model by employing the Gamma-Ray Spectral Fitting Package (RMFIT V4.3.2)⁸ for 14 GRBs⁹. The spectroscopic or photometric redshifts of GRBs are obtained from the *Swift* database¹⁰ and the webpage of J. Greiner¹¹, which compiles and published papers.

We identify a total 187 GRBs with redshift measured (with a cutoff at GRB230818). In order to obtain suitable long GRB data with redshifts, we excluded some GRBs based on the following criteria:

³ <https://heasarc.gsfc.nasa.gov/W3Browse/fermi/fermigbrst.html>

⁴ For a very wide energy band of Fermi-GBM, the GRBs prompt emission spectrum $\Phi(E)$ can be usually best fitted by the BAND model as the spectral parameters (the observed peak energy E_p , the low and high energy spectral index: α and β) (Zhang, Huang, & Zou. 2023), which is an empirical spectral function with a broken power law (Band et al. 1993):

$$\Phi(E) = A \begin{cases} \left(\frac{E}{100\text{keV}}\right)^\alpha e^{-(2+\alpha)\frac{E}{E_p}}, & \text{if } E \leq \frac{\alpha-\beta}{2+\alpha} E_p \\ \left(\frac{E}{100\text{keV}}\right)^\beta \left(\frac{\alpha-\beta}{2+\alpha} E_p\right)^{(\alpha-\beta)} e^{(\beta-\alpha)}, & \text{otherwise.} \end{cases} \quad (1)$$

where the normalization parameter A is chosen to ensure continuity at the break and to match the observed burst brightness. In this work, the BAND function which has been used in many previous analysis (Wang et al. 2016; Demianski et al. 2017a; Amati et al. 2019; Montiel et al. 2021; Jia et al. 2022) is chosen as the reference model for simplicity. It should be noted that other spectral models (COMP: An exponentially attenuated power law, namely "comptonized", SBPL: A smoothly broken power law and PLAW: A single power law) (Poolakkil et al. 2021) can be chose to fit the spectra of GRBs. Poolakkil et al. (2021) have used 10 years of GBM data and the known redshift for ~ 130 GRBs to obtain different rest-frame energetics with the BAND model and the COMP model, respectively.

⁵ GRB180728A, GRB181020A, GRB190114C, GRB190324A, GRB190829A, GRB200524A, GRB200613A, GRB200829A, GRB201020B, GRBGRB201216C, GRB210204A, GRB210619B, GRB211023A, GRB220101A, GRB220107A, GRB220527A, GRB220627A, GRB230204B, GRB230812B.

⁶ <https://gcn.nasa.gov/circulars>

⁷ <https://heasarc.gsfc.nasa.gov/FTP/fermi/data/gbm/bursts/>

⁸ <https://fermi.gsfc.nasa.gov/ssc/data/p7rep/analysis/rmfit/>

⁹ GRB181010A, GRB190613A, GRB190719C, GRB191011A, GRB201020A, GRB201021C, GRB210104A, GRB210610A, GRB210610B, GRB210722A, GRB210731A, GRB220521A, GRB221226B, GRB230818A.

¹⁰ https://swift.gsfc.nasa.gov/archive/grb_table.html

¹¹ <http://www.mpe.mpg.de/~jcg/grbgen.html>

(i) Short GRBs: There are 26 short GRBs¹² from the identified 187 GRBs with redshift.

(ii) Unsafe Redshifts: There are 2 GRBs¹³ with only limits and one GRB¹⁴ with two possible redshifts.

(iii) Significant uncertainties in the spectral parameters: There are 7 GRBs¹⁵ with significant uncertainties of E_p which only present poor contribution to fitting procedure.

By discarding the above short GRBs, GRBs with unsafe redshifts and significant uncertainties in the spectral parameters, we can obtain 151 long GRBs with identified redshift at $0.0785 \leq z \leq 8.2$ to be considered as the FULL sample. More careful selections should be required to reduce the uncertainties of GRB data and redshifts measured.

(iv) Photometric Redshifts: There are 8 GRBs¹⁶ with redshift obtained through photometric method, relying on photometric information rather than spectral features, leading to differences between measured values and actual redshifts.

(v) Uncertain Redshifts: There are 2 GRBs¹⁷ with uncertain redshifts.

(vi) The peak flux selection: We also considered the impact of peak flux selection with a peak flux threshold in the trigger energy range that is typically 50% higher than the trigger threshold (Atteia et al. 2017). There are 22 GRBs with a 1s peak flux in the energy range (50 – 300keV) lower than 1.5 times the detection threshold of $P = 0.70\text{ph cm}^{-2} \text{s}^{-1}$, in which 18 GRBs are not counted twice.

If further discarding GRBs with photometric redshifts and uncertain redshifts, and GRBs lower than the peak flux selection, we can get a *Fermi*-GBM GRB sample consists of 123 long GRBs to be considered as the GOLD sample from the FULL sample of 151 long GRBs with identified redshift, which covers from GRB 080804 to GRB 230818A at the redshift range $0.0785 \leq z \leq 5.6$. The bursts not included in the GOLD and FULL sample are shown in Table 1. The redshift distribution for the GOLD and FULL samples are shown in Figure 1. For comparison, the M2021 sample (Montiel et al. 2021) of 74 GRBs at $0.117 \leq z \leq 5.283$ are also shown in Figure 1. In Appendix, we list the *Fermi*-GBM GRBs with

¹² It is worth noting that 2 GRBs with $T_{90} > 2\text{s}$ should be short GRBs: GRB170817A (GBM trigger 170817529 with $T_{90} = 2.048$)(Goldstein et al. 2017) and GRB 180618A (GBM trigger 180618030 with $T_{90} = 3.712$)(Jordana-Mitjans et al. 2022).

¹³ For GRB100802A, the data are not sufficient to estimate a definite photometric redshift, but place an upper limit redshift of $z < 3.1$ (Perley et al. 2016). For GRB190530A, any significant absorption or emission lines in the low-resolution spectrum is not detected, but an upper limit of $z < 2.2$ has been inferred based on the detected continuum (Heintz et al. 2019).

¹⁴ For GRB110721A, the redshift is not known for spectroscopy of the counterpart suggested two possible redshifts, $z = 0.382$ and 3.512 (Iyyani et al. 2013).

¹⁵ The relative error of E_{peak} of GRB080928, GRB100728B, GRB110128A, GRB120729, GRB150120, GRB160620, and GRB221009 are significant large.

¹⁶ GRB080916, GRB120922, GRB131229, GRB151111, GRB151229, GRB161001, GRB180418, GRB200829.

¹⁷ For GRB140713A, Higgins et al. (2019) obtained $z = 0.935$ with the emission spectrum of the likely host galaxy; however, Schroeder et al. (2022) obtained $z = 0.935 \pm 0.002$ with identified [O II] and [O III]. For GRB190613A, the redshift due to Lyman alpha at $z = 2.78$ is tentative currently due to the lack of corroborating features (Cunningham & SEDM Team 2019).

Table 1. Burst Not Included in the FULL sample and the GOLD sample.

GRB	Cause	Note	GRB	Cause	Note	GRB	Cause	Note
080905A	short	$T_{90}=0.96$	120729A	SU	$E_{p,obs}^* = 6.614$	170817A	short	$T_{90}=2.048$
080905B	low-flux ^a	$P = 0.5815$	120922A	photometric- z	$z=3.1(\text{ph})$	171222A	low-flux	$P = 0.1903$
080916C	photometric- z	$z=4.35(\text{ph})^b$	121211A	low-flux	$P = 0.5809$	180418A	photometric- z	$z=1.55(\text{phh})$
080928	SU ^c	$E_{p,obs}^* = 3.395$	130515A	short	$T_{90}=0.256$	180618A	short	$T_{90}=3.712$
081109A	low-flux	$P = 0.7858$	130612A	low-flux	$P = 0.2384$	180727A	short	$T_{90}=0.896$
090423	low-flux	$P = 0.5781$	130716A	short	$T_{90}=0.768$	180805B	short	$T_{90}=0.96$
090510	short	$T_{90}=0.96$	131004A	short	$T_{90}=1.152$	181010A	low-flux	$P = 0.0541$
090927	short	$T_{90}=0.512$	131229A	photometric- z	$z=1.04(\text{phh})^b$	190530A	unsafe- z	$z < 2.2$
100117A	short	$T_{90}=0.256$	140304A	low-flux	$P = 0.9886$	190613A	uncertain- z	$z=2.78(?)$
100206A	short	$T_{90}=0.176$	140623A	low-flux	$P = 0.5639$	191011A	low-flux	$P = 0.7477$
100625A	short	$T_{90}=0.24$	140713A	uncertain- z	$z = 0.935 \pm 0.002$	191031D	short	$T_{90}=0.256$
100728B	SU	$E_{p,obs}^* = 2993$	150101B	short	$T_{90}=0.08$	200219A	short	$T_{90}=1.152$
100802A	unsafe- z	$z < 3.1^d$	150120A	SU	$E_{p,obs}^* = 16.73$	200411A	short	$T_{90}=1.44$
101219B	low-flux	$P = 0.6811$	151111A	photometric- z	$z=3.5(\text{ph})$	200826A	short	$T_{90}=1.136$
101224A	short	$T_{90}=1.728$	151229A	photometric- z	$z=1.4(\text{phh})$	200829A	photometric- z	$z=1.25(\text{phh})$
110106B	low-flux	$P = 0.8208$	160408A	short	$T_{90}=1.056$	201020A	low-flux	$P = 0.612$
110128A	SU	$E_{p,obs}^* = 139.7$	160623A	SU	$E_{p,obs}^* = 4.632$	201021C	low-flux	$P = 0.549$
110721A	unsafe- z	$z=3.512(?)^d$	160624A	short	$T_{90}=0.384$	201221D	short	$T_{90}=0.144$
110818A	low-flux	$P = 0.7446$	160821B	short	$T_{90}=1.088$	210323A	short	$T_{90}=0.96$
111107A	low-flux	$P = 0.563$	161001A	photometric- z	$z=0.67(\text{phh})$	221009A	SU	$E_{p,obs}^* = 2.35$
111117A	short	$T_{90}=0.432$	170113A	low-flux	$P = 0.5287$			
120118B	low-flux	$P = 0.7201$	170127B	short	$T_{90}=1.728$			

^a low-flux: The 1s peak flux in the energy range (50 – 300keV) lower than 1.5 times the detection threshold of $P = 0.70\text{ph cm}^{-2} \text{s}^{-1}$.

^b SU: Significant uncertainties in the spectral parameters. The relative error of E_p ($E_{p,obs}^*$) is significant large.

^c ph=photometric redshift; phh=photometric redshift of host galaxy;

^d "<"=upper limit redshift; "?"=controversial redshift;

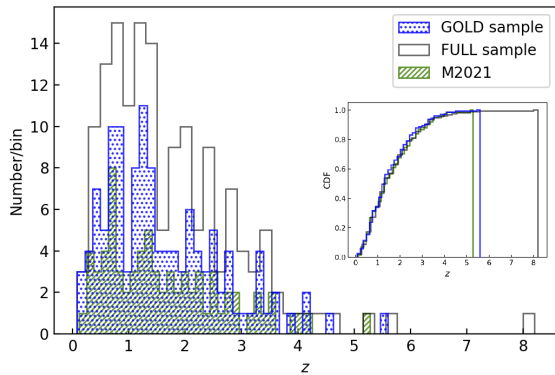


Figure 1. The redshift distribution for the Fermi-GBM GRBs with the FULL sample (*black histogram*) of 151 GRBs at $0.0785 \leq z \leq 8.2$, the GOLD sample (*blue histogram*) of 123 GRBs at $0.0785 \leq z \leq 5.6$, and the M2021 sample (*green histogram*) of 74 GRBs at $0.117 \leq z \leq 5.283$. The cumulative distribution function (CDF) of the FULL sample (*black curve*), the GOLD sample (*blue curve*), and the M2021 sample (*green curve*) are indicated in the inset, respectively.

the FULL and GOLD samples together with the redshifts (z), the T_{90} parameter; as well as the spectral parameters

(E_p , α , β) and the measured bolometric fluence S_{bolo} with the associated errors in Table A1 and Table A2.¹⁸

3 CALIBRATION OF AMATI RELATION

The Amati relation relates the spectral peak energy ($E_{p,i}$) and the isotropic energy (E_{iso}), which can be expressed in the functional form,

$$\log_{10}\left(\frac{E_{\text{iso}}}{\text{erg}}\right) = a + b \log_{10}\left(\frac{E_{p,i}}{300\text{keV}}\right) \quad (4)$$

where a and b are free parameters to be determined from the data, the spectral peak energy in the GRB cosmological rest

¹⁸ S_{bolo} can be computed from the observed fluence S multiplying by the k -value in the standard rest-frame energy band $1 - 10^4\text{keV}$ (Poolakkil et al. 2021),

$$k = \frac{\int_{1/(1+z)}^{10^4/(1+z)} E\Phi(E)dE}{\int_{E_{\text{min}}}^{E_{\text{max}}} E\Phi(E)dE} \quad (2)$$

here the detection limits of GBM: $E_{\text{min}} = 10\text{keV}$ and $E_{\text{max}} = 1000\text{keV}$. The error of k can be calculate by using the following error propagation formula:

$$(\sigma_k)^2 = \left(\frac{\partial k}{\partial \alpha}\right)^2(\sigma_\alpha)^2 + \left(\frac{\partial k}{\partial \beta}\right)^2(\sigma_\beta)^2 + \left(\frac{\partial k}{\partial A}\right)^2(\sigma_A)^2 + \left(\frac{\partial k}{\partial E_p}\right)^2(\sigma_{E_p})^2 \quad (3)$$

frame $E_{p,i} = E_p(1+z)$, and E_{iso}

$$E_{\text{iso}} = 4\pi d_L^2 S_{\text{bolo}}(1+z)^{-1} \quad (5)$$

The luminosity distance d_L , for a flat spatially universe, can be calculated by

$$d_L^{\text{cal}} = c(1+z) \int_0^z \frac{dz'}{H(z')}. \quad (6)$$

We use a Gaussian process to reconstruct $H(z)$ at redshift z with the observational data. Gaussian process (Seikel et al. 2012) is a nonparametric technique, in which the reconstruct only depends on the chosen kernel function and the data observed. In the Gaussian process, the reconstructed function \mathbf{f}_* from the data \mathbf{y} which is known from observations can be described with its mean function and covariance function:

$$\begin{aligned} \bar{\mathbf{f}}_* &= \boldsymbol{\mu}_* + K(\mathbf{Z}_*, \mathbf{Z}) [K(\mathbf{Z}, \mathbf{Z}) + \mathbf{C}]^{-1} (\mathbf{y} - \boldsymbol{\mu}) \\ \text{cov}(\mathbf{f}_*) &= K(\mathbf{Z}_*, \mathbf{Z}_*) - K(\mathbf{Z}_*, \mathbf{Z}) [K(\mathbf{Z}, \mathbf{Z}) + \mathbf{C}]^{-1} K(\mathbf{Z}, \mathbf{Z}_*) \end{aligned} \quad (7)$$

where $\boldsymbol{\mu}_*$ is the priori assumed mean of \mathbf{f}_* . For a set of input points $\mathbf{Z} = \{z_i\}$, the covariance matrix $K(\mathbf{Z}, \mathbf{Z})$ is given by $[K(\mathbf{Z}, \mathbf{Z})]_{ij} = \mathbf{k}(z_i, z_j)$. In this work, we use the squared exponential covariance function (Seikel et al. 2012): $\mathbf{k}(z, \tilde{z}) = \sigma_f^2 \exp(-\frac{(z-\tilde{z})^2}{2l^2})$, with the two hyperparameters l and σ_f which can be optimized and determined by maximizing the log marginal likelihood.

We use the public python package GaPP¹⁹ with the observational data. The latest 32 OHD in the range $0.07 < z < 1.965$ (see Moresco et al. (2022); Li, Zhang & Liang (2023) and reference therein) are used to reconstruct $H(z)$. The total covariance matrix²⁰ as the combination of the statistical and systematic part (Moresco et al. 2020) of 15 $H(z)$ estimates from the measurements (Moresco et al. 2012, 2016; Moresco 2015) in the range $0.179 < z < 1.965$ has to be taken into account. In order to calibrate the Amati relation, we choose $z = 1.4$ (Liang et al. 2022; Li, Zhang & Liang 2023) to divide GRBs into low- and high-redshift sample. The reconstructed results through Gaussian process with the 1σ uncertainty from OHD are plotted in Figure 2.

The Markov Chain Monte Carlo (MCMC) of Python package emcee (Foreman-Mackey et al. 2013) is used to calibrate the Amati relation at $z < 1.4$ by using the fitting methods with the likelihood function proposed by D'Agostini (2005)²¹ and Reichart et al. (2001)²² which has the advantage of not requiring the arbitrary choice of an independent variable in x -axis and y -axis.

We also take into account the possible intrinsic scatter of

¹⁹ <https://github.com/astrobengaly/GaPP>

²⁰ https://gitlab.com/mmoresco/CCcovariance/-/tree/master?ref_type=heads

²¹ The likelihood function proposed by D'Agostini (2005) is: $\mathcal{L}_D \propto \prod_{i=1}^{N_1} \frac{1}{\sigma} \times \exp\left[-\frac{[y_i - y(x_i, z_i; a, b)]^2}{2(\sigma_{\text{int}}^2 + \sigma_{y,i}^2 + b^2 \sigma_{x,i}^2)}\right]$, with σ_{int} means the intrinsic scatter.

²² The likelihood function proposed by Reichart et al. (2001) can be written as (Lin et al. 2015; Li, Zhang & Liang 2023): $\mathcal{L}_R \propto \prod_{i=1}^{N_1} \frac{\sqrt{1+b^2}}{\sigma} \times \exp\left[-\frac{[y_i - y(x_i, z_i; a, b)]^2}{2(\sigma_{\text{int}}^2 + \sigma_{y,i}^2 + b^2 \sigma_{x,i}^2)}\right]$, here $\sigma_{\text{int}} = \sqrt{\sigma_{y,\text{int}}^2 + b^2 \sigma_{x,\text{int}}^2}$, in which $\sigma_{y,\text{int}}^2$ and $\sigma_{x,\text{int}}^2$ are the intrinsic scatter along the axes.

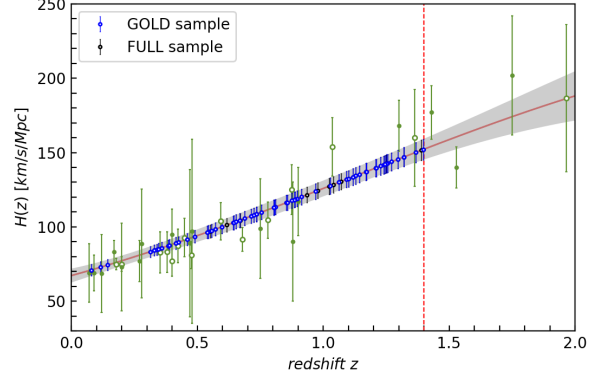


Figure 2. The reconstructed results from OHD through Gaussian process. The green cycles and dots indicate the 15 OHD with the full covariance matrices and the other 17 OHD without covariance, respectively. The red curve presents the reconstructed function with the 1σ uncertainty from OHD by taking into account the full covariance matrices. The GRBs with the FULL sample (black cycles) and the GOLD sample (blue cycles) at $z < 1.4$ are reconstructed from OHD through the Gaussian process. The red dotted line denotes $z = 1.4$.

the data with respect to the linear fit and the measurement errors in both variables and employ the Python module Nemmen et al. (2012)²³ by the Bivariate Correlated Errors and intrinsic Scatter (BCES) method (Akritas & Bershady 1996). The calibration results of the Amati relation by the three methods are summarized in Table 2. We find that the fitting results by the likelihood function (D'Agostini 2005) are consistent with the ones by BCES($y|x$); and the fitting results by the likelihood function (Reichart et al. 2001) are consistent with the ones by BCES-orthogonal²⁴. We plot the Amati relation with the FULL and GOLD samples at $z < 1.4$ by the BCES-orthogonal method in Figure 3. The results of the intercept a and the slope b with the FULL and GOLD sample are well consistent at 1σ , while the difference of the slope b between the FULL and GOLD sample is apparently significant, in which the value of the slope b with the GOLD sample is close to the theoretical value of the slope with the Amati relation: 2. Our results at $z < 1.4$ by the BCES-orthogonal method are consistent with Montiel et al. (2021), which calibrated the Amati relation with the OHD at $z < 1.43$.

From Table 2 and Figure 3, we find the Amati relation of GRBs at $z < 1.4$ looks significantly more dispersed and flat to most previous works. This flatness can be quantified by the surprising value of the slope obtained. In order to investigate whether this flatness and high dispersion are due to the rather small sample of GRBs at $z < 1.4$ or is a characteristic of the whole Fermi/GBM sample, we use the fitting results with the whole FULL and GOLD samples up to high redshifts by the BCES-orthogonal method. For the uncertainties of GP

²³ <https://github.com/rsnemmen/BCES>

²⁴ The BCES-Orthogonal least squares: line that minimizes orthogonal distances, which should be used when it is not clear which variable should be treated as the independent one, whereas the BCES-bisector approach which bisects the $y|x$ and $x|y$ is self-inconsistent (Hogg, Bovy, & Lang 2010).

Table 2. Calibration results (the intercept a , the slope b , the intrinsic scatter σ_{int} , and the covariance matrix by BCES methods) of the Amati relation with the FULL sample and the GOLD sample at $z < 1.4$ by D’Agostini method and the Reichart method (Reichart et al. 2001; D’Agostini 2005) and the BCES methods (Akritas & Bershady 1996) with BCES($y|x$) and BCES-Orthogonal least squares.

Sample/Methods	a	b	σ_{int}/cov
FULL/D’Agostini	52.35 ± 0.08	0.88 ± 0.18	$0.65^{+0.05}_{-0.06}$
GOLD/D’Agostini	52.41 ± 0.08	0.83 ± 0.18	$0.61^{+0.05}_{-0.07}$
FULL/Reichart	52.42 ± 0.11	$2.52^{+0.40}_{-0.19}$	0.50 ± 0.29
GOLD/Reichart	52.46 ± 0.12	$2.36^{+0.38}_{-0.33}$	0.50 ± 0.29
FULL/BCES($y x$)	52.33 ± 0.08	0.92 ± 0.18	$\begin{pmatrix} 0.006 & 0.003 \\ 0.003 & 0.033 \end{pmatrix}$
GOLD/BCES($y x$)	52.39 ± 0.08	0.86 ± 0.18	$\begin{pmatrix} 0.006 & 0.002 \\ 0.002 & 0.032 \end{pmatrix}$
FULL/BCES-Ort	52.39 ± 0.11	2.46 ± 0.58	$\begin{pmatrix} 0.013 & -0.003 \\ -0.003 & 0.331 \end{pmatrix}$
GOLD/BCES-Ort	52.43 ± 0.11	2.16 ± 0.57	$\begin{pmatrix} 0.012 & -0.007 \\ -0.007 & 0.324 \end{pmatrix}$

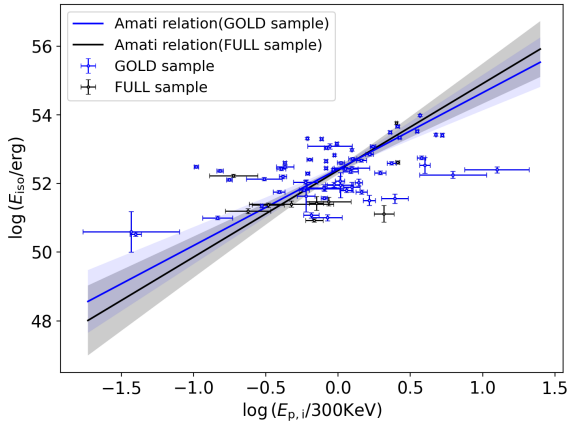


Figure 3. The best-fit calibration of Amati relation by BCES-orthogonal method with the FULL sample (*black cycles*) and the GOLD sample (*blue cycles*) at $z < 1.4$. For the FULL sample, the Spearman’s rank coefficient of the correlation is $\rho = 0.49$, and the P-value = 6.9×10^{-6} . For the GOLD sample, the Spearman’s rank coefficient of the correlation is $\rho = 0.45$, and the P-value = 1.82×10^{-4} .

reconstruction extrapolating to $z > 1.4$ are very large, we assume the Λ CDM model to calculate the best-fit calibration of Amati relation by BCES-orthogonal method with the FULL and the GOLD samples at all z , which are shown in Figure 4. We find the value of the slope b is more close to the theoretical value of the slope with the Amati relation: 2. The Spearman’s rank correlation coefficients are larger than the ones at low redshift. These results indicate that this flatness and high dispersion at low redshift for the Fermi sample are due to the rather small sample of GRBs.

In order to take into account the measurement errors in

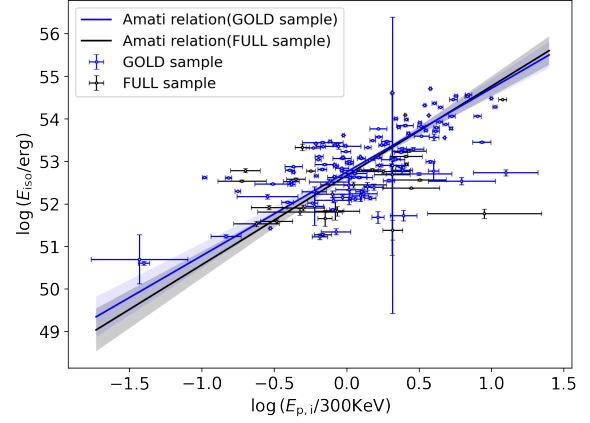


Figure 4. The best-fit calibration of Amati relation by BCES-orthogonal method with the FULL sample (*black cycles*) and the GOLD sample (*blue cycles*) at all z by assuming the Λ CDM model from Pantheon+ ($\Omega_m = 0.334, H_0 = 73.6 \text{ km/s/Mpc}$) (Brout et al. 2022). FULL/BCES-Ort: $a = 52.67 \pm 0.08, b = 2.09 \pm 0.35$, GOLD/BCES-Ort: $a = 52.75 \pm 0.09, b = 1.96 \pm 0.37$. The Spearman’s rank coefficient of the correlation are $\rho = 0.60$ and $\rho = 0.63$, and the P-value are 4.75×10^{-17} , 4.31×10^{-16} for the FULL and GOLD samples, respectively.

both variables, we use the calibration results of the BCES-orthogonal method to constrain cosmological models.

4 CONSTRAINING COSMOLOGICAL MODELS

We assume that the calibration results of the Amati relation at low-redshift are valid at high-redshift to build the GRB Hubble diagram. The Hubble diagram of the *Fermi* sample is plotted in Fig. 5. The observable distance moduli ($\mu = 5 \log \frac{d_L}{\text{Mpc}} + 25$) of GRBs can be calculated by the calibration results of the Amati relation,

$$\mu_{\text{GRB,obs}} = 25 + \frac{5}{2} \left[a + b \log E_{p,i} - \log \frac{4\pi S_{\text{bolo}}}{(1+z)} \right] \quad (8)$$

The propagated uncertainties of the distance moduli is,

$$\sigma_{\mu_{\text{GRB}}}^2 = \sigma_{\text{cal}}^2 + \left(\frac{\partial \mu_{\text{GRB}}}{\partial E_{p,i}} \right)^2 \sigma_{E_{p,i}}^2 + \left(\frac{\partial \mu_{\text{GRB}}}{\partial S_{\text{bolo}}} \right)^2 \sigma_{S_{\text{bolo}}}^2 \quad (9)$$

where σ_{cal}^2 is the uncertainties from calibration parameters (a, b) of the Amati relation,

$$\sigma_{\text{cal}}^2 = \left(\frac{\partial \mu_{\text{GRB}}}{\partial a} \right)^2 \sigma_a^2 + \left(\frac{\partial \mu_{\text{GRB}}}{\partial b} \right)^2 \sigma_b^2 + 2 \left(\frac{\partial \mu_{\text{GRB}}}{\partial a} \right) \left(\frac{\partial \mu_{\text{GRB}}}{\partial b} \right) \sigma_{ab} \quad (10)$$

here σ_{ab} is the non-diagonal matrix elements of \mathbf{cov} .

We use the GRB data in the Hubble diagram at high-redshift to constrain cosmological models. The χ^2 of the GRB data is

$$\chi_{\text{GRB}}^2 = \Delta \mu_{\text{GRB}} \mathbf{C}_{\text{GRB}}^{-1} \Delta \mu_{\text{GRB}} \quad (11)$$

here \mathbf{C}_{GRB} is the diagonal matrix containing of σ_{μ}^2 (Montiel et al. 2021) for simplicity, $\Delta \mu_{\text{GRB}} = \mu_{\text{GRB,obs}} - \mu_{\text{th}}$ is the

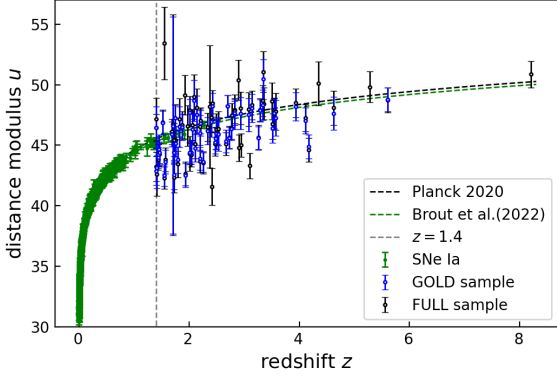


Figure 5. GRB Hubble diagram of the FULL sample (*black cycles*) and the GOLD sample (*blue cycles*). The green dots represent Pantheon+ SNe Ia. The green dashed curve and the black dashed curve are the predicted values of distance modulus for a flat Λ CDM model from Pantheon+ ($\Omega_m = 0.334$, $H_0 = 73.6$ km/s/Mpc) (Brout et al. 2022), and CMB ($\Omega_m = 0.315$, $H_0 = 67.4$ km/s/Mpc) (Planck Collaboration 2020), respectively. The gray dotted line denotes $z = 1.4$.

vector of the differences between the observable and theoretical value of the distance moduli for the GRBs. The theoretical distance modulus is $\mu_{\text{th}}(z) \equiv 5 \log_{10} D_L(z) + \mu_0$, where $\mu_0 \equiv 42.38 - 5 \log h$, h is the Hubble constant H_0 in units 100 km/s/Mpc, and the unanchored luminosity distance is

$$D_L(z) = (1+z) \int_0^z \frac{dz'}{E(z')} \quad (12)$$

here $E(z) = \frac{H(z)}{H_0}$ is the unanchored Hubble parameter which can be determined by the dark energy (DE) models. Assuming a flat universe, we consider Λ CDM model, w CDM model, and the well-known Chevallier-Polarski-Linder (CPL) model (Chevallier & Polarski 2001; Linder 2003) in this work. The Friedmann equation is given by

$$E(z) \equiv \begin{cases} \sqrt{\Omega_m(1+z)^3 + \Omega_{\text{DE}, \Lambda\text{CDM model}}} \\ \sqrt{\Omega_m(1+z)^3 + \Omega_{\text{DE}}(1+z)^{3(1+w_0)}}, w\text{CDM model} \\ \sqrt{\Omega_m(1+z)^3 + \Omega_{\text{DE}}(1+z)^{3(1+w_0+w_a)} \exp\left(-\frac{3w_0 z}{1+z}\right)}, \text{CPL} \end{cases} \quad (13)$$

We also combine the Pantheon+ SNe Ia sample (Scolnic et al. 2022) to constrain cosmological models with the GRB sample. The χ^2 of the SNe Ia is

$$\chi_{\text{SN}}^2 = \Delta\mu_{\text{SN}}^T \mathbf{C}_{\text{SN}}^{-1} \Delta\mu_{\text{SN}} \quad (14)$$

where $\Delta\mu_{\text{SN}} \equiv \mu_{\text{th}} - \mu_{\text{SN,obs}}$ is the module of the vector of residuals, \mathbf{C}_{SN} is the covariance matrix (Brout et al. 2022) of 1701 SNe Ia. The total χ^2 with SNe Ia and GRB is given by

$$\chi_{\text{tot}}^2 = \chi_{\text{GRB}}^2 + \chi_{\text{SNe}}^2 \quad (15)$$

We use the MCMC method of Python package emcee (Foreman-Mackey et al. 2013) to minimize the χ^2 . In order to constrain DE models, we use the 15 years of the *Fermi*-GBM GRBs with the FULL sample and the GOLD sample at high-redshift $z \geq 1.4$. For comparison, we also use GRB

data at high-redshift from M2021 (Montiel et al. 2021) with the 74 GRBs (2008-2019) at $0.117 \leq z \leq 5.283$ in the same calibration method through Gaussian process from the latest OHD.

We set $H_0 = 73$ km/s/Mpc²⁵ to constrain only with GRBs at $z \geq 1.4$ including the GOLD, FULL and M2021 sample. The results are summarized in Table 3. For the flat Λ CDM model (Figure 6), we obtain $\Omega_m = 0.386^{+0.014}_{-0.004}$ and $\Omega_m = 0.385^{+0.015}_{-0.005}$ with the GOLD and FULL sample, respectively; for the flat w CDM model (Figure 7), we obtain $w_0 = -0.87^{+0.07}_{-0.02}$ and $w_0 = -0.88^{+0.08}_{-0.02}$ with the GOLD and FULL sample, respectively; for the CPL model (Figure 8), we obtain $w_a = -1.25^{+0.35}_{-0.13}$ and $w_a = -1.24^{+0.33}_{-0.13}$ with the GOLD and FULL sample, which favours a possible DE evolution at the 1σ confidence region for all cases only with GRBs at $z \geq 1.4$. Our results with the GOLD and FULL sample are almost identical, which are more stringent than the results of M2021 sample. We find that the values of Ω_m with the GOLD and FULL sample for the flat Λ CDM model is larger than the result of M2021 sample: $\Omega_m = 0.370^{+0.030}_{-0.009}$, which are much less than ones obtained in previous analyses only with A219 and A118 GRBs at high-redshift: $\Omega_m \sim 0.5$ (Liang et al. 2022).

The joint constraints with Pantheon+ SNe Ia and the GOLD, FULL and M2021 sample at high-redshift are summarized in Table 4. For the flat Λ CDM model (Figure 9): $\Omega_m = 0.354 \pm 0.018$, $H_0 = 73.05 \pm 0.2$ and $\Omega_m = 0.353 \pm 0.018$, $H_0 = 73.06 \pm 0.2$ with the GOLD and FULL sample, respectively, which are slightly different with ones obtained with the Pantheon+ sample $\Omega_m = 0.334 \pm 0.018$, $H_0 = 73.6 \pm 1.1$ for the flat Λ CDM model (Brout et al. 2022); for the flat w CDM model (Figure 10): $w_0 = -1.22^{+0.18}_{-0.15}$ and $w_0 = -1.21^{+0.18}_{-0.15}$ with the GOLD and FULL sample, respectively; for the CPL model (Figure 11): $w_a = -1.12^{+0.45}_{-0.83}$ and $w_a = -1.16^{+0.66}_{-0.80}$ with the GOLD and FULL sample, respectively. Our results with the GOLD and FULL sample are almost identical, which are more stringent than the results of M2021 sample. We find our results with the GOLD, FULL sample and Pantheon+ sample that are quite different with the previous analyses obtained from A118 sample at high-redshift and Pantheon sample: $\Omega_m = 0.286 \pm 0.012$, $H_0 = 69.70 \pm 0.22$ for the flat Λ CDM model (Li, Zhang & Liang 2023).

Finally, we compare these dark energy models with Akaike Information Criterion (AIC), Bayesian Information Criterion (BIC), which defined by

$$\text{AIC} = -2 \ln \mathcal{L}_{\text{max}} + 2k, \quad \text{BIC} = -2 \ln \mathcal{L}_{\text{max}} + k \ln N \quad (16)$$

where \mathcal{L}_{max} is the maximum likelihood. The value of ΔAIC and ΔBIC are given by

$$\Delta\text{AIC} = \Delta\chi_{\text{min}}^2 + 2\Delta k, \quad \Delta\text{BIC} = \Delta\chi_{\text{min}}^2 + \Delta k \ln N \quad (17)$$

In the Gaussian cases, $\chi_{\text{min}}^2 = -2 \ln \mathcal{L}_{\text{max}}$. The results of the value of ΔAIC and ΔBIC with respect to the reference model (the Λ CDM model) are summarized in Table 3 and 4. We find

²⁵ If just to make the comparison with the cosmological parameters obtained by joining GRBs with SNe more straightforward, it would be better to assume $H_0 = 73$ km/s/Mpc for the derivation of cosmological parameters based on GRBs only. Of course, this should not impact significantly the result, but it would allow a more consistent comparison.

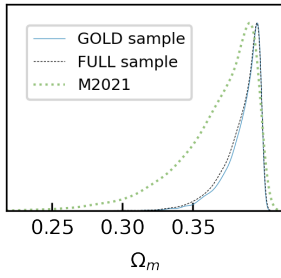


Figure 6. Constraints on parameters of Ω_m for the flat Λ CDM model with GRBs at $z \geq 1.4$ from the FULL sample (black dashed curves), the GOLD sample (blue curves), and the M2021 sample (green dotted curves), respectively.

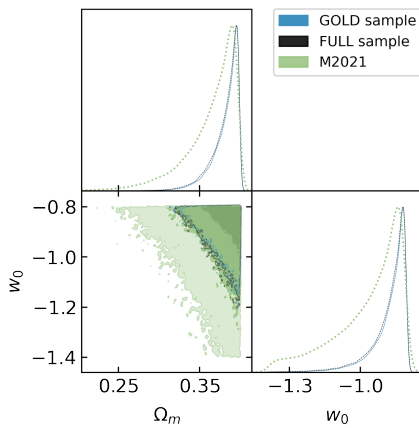


Figure 7. Constraints on parameters of Ω_m and w_0 for the flat w CDM model with GRBs at $z \geq 1.4$ from the FULL sample (black dashed curves), the GOLD sample (blue curves), and the M2021 sample (green dotted curves), respectively.

that Λ CDM model is preferred with respect to the w CDM and the CPL models, which is consistent with the previous analyses (Amati et al. 2019; Montiel et al. 2021) and (Li, Zhang & Liang 2023).

5 CONCLUSION AND DISCUSSIONS

In the present work, we compile a *Fermi* sample of the long GRBs from *Fermi* observations with 15 years of the Fermi-GBM catalogue with identified redshift, in which the GOLD sample contains 123 long GRBs at $z \leq 5.6$ and the FULL sample contains 151 long GRBs with redshifts at $z \leq 8.2$. The Amati relation are calibrated from the latest OHD with the CC method using a Gaussian Process at $z < 1.4$ to obtain GRBs at $z \geq 1.4$ which can be used to constrain cosmological models. By the MCMC method with the GRBs in the GOLD and FULL sample at $z \geq 1.4$ and the Pantheon+ sample, we obtain $\Omega_m = 0.354 \pm 0.018$, $H_0 = 73.05 \pm 0.2$ and $\Omega_m = 0.353 \pm 0.018$, $H_0 = 73.06 \pm 0.2$ for the flat Λ CDM model; $w_0 = -1.22^{+0.18}_{-0.15}$ and $w_0 = -1.21^{+0.18}_{-0.15}$ for the flat w CDM model; $w_a = -1.12^{+0.45}_{-0.83}$ and $w_a = -1.16^{+0.66}_{-0.80}$ for the CPL model.

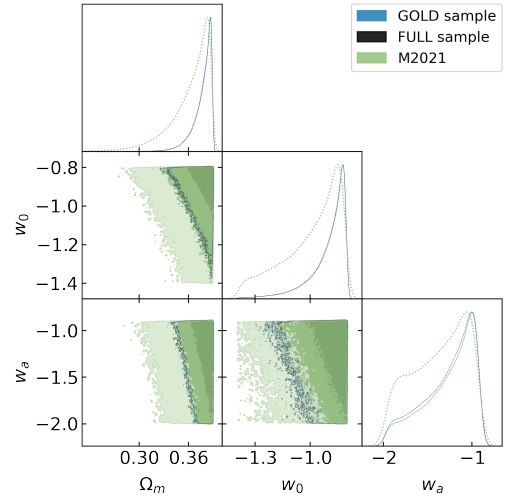


Figure 8. Constraints on parameters of Ω_m , w_0 and w_a for the flat CPL model with GRBs at $z \geq 1.4$ from the FULL sample (black dashed curves), the GOLD sample (blue curves), and the M2021 sample (green dotted curves) respectively.

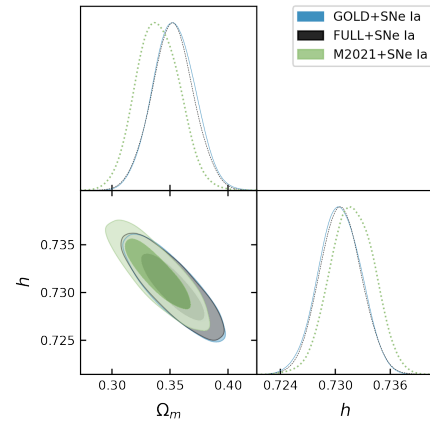


Figure 9. Constraints on parameters of Ω_m , h for the flat Λ CDM model with SNe Ia and GRBs at $z \geq 1.4$ from the FULL sample (black dashed curves), the GOLD sample (blue curves), and the M2021 sample (green dotted curves), respectively.

We also find that Λ CDM model is preferred with respect to the w CDM and the CPL models.

It should be note that there is a debate as to whether the Amati relation is an intrinsic effect or the result of detection biases (Butler et al. 2007; Butler, Kocevski, & Bloom 2009; Butler, Bloom, & Poznanski 2010) and the instrumental selection biases (Ghirlanda et al. 2008; Nava et al. 2012b), which cannot be responsible for the existence of the spectral-energy correlations. Our sample in this work originate from a single catalogue, thus avoiding selection biases and other instrument-associated systematics. Moreover, the Amati relation could arguably evolve with redshift, which have been discussed in many works (Demianski et al. 2017a; Tang et al. 2021; Khadka et al. 2021). Liu et al. (2022a,b) proposed the improved Amati relation by accounting for evolutionary effects via copula to found that a redshift evolutionary cor-

Table 3. The constraints only with GRBs at $z > 1.4$ in the FULL sample, the GOLD sample, and the M2021 sample for the flat Λ CDM model, the flat w CDM model, and the CPL model by setting $H_0 = 73\text{km/s/Mpc}$.

Data Set	Models	Ω_m	w_0	w_a	ΔAIC	ΔBIC
GOLD sample	Λ CDM	$0.386^{+0.014}_{-0.004}$	-	-	0	0
	w CDM	$0.383^{+0.017}_{-0.005}$	$-0.87^{+0.07}_{-0.02}$	-	0.55	1.56
	CPL	$0.379^{+0.011}_{-0.002}$	$-0.89^{+0.09}_{-0.02}$	$-1.25^{+0.35}_{-0.13}$	1.15	2.91
FULL sample	Λ CDM	$0.385^{+0.015}_{-0.005}$	-	-	0	0
	w CDM	$0.382^{+0.018}_{-0.005}$	$-0.88^{+0.08}_{-0.02}$	-	0.77	2.90
	CPL	$0.378^{+0.012}_{-0.003}$	$-0.90^{+0.10}_{-0.02}$	$-1.24^{+0.33}_{-0.13}$	1.58	3.86
M2021	Λ CDM	$0.368^{+0.032}_{-0.011}$	-	-	0	0
	w CDM	$0.365^{+0.035}_{-0.010}$	$-0.96^{+0.16}_{-0.05}$	-	1.15	3.25
	CPL	$0.363^{+0.027}_{-0.007}$	$-0.99^{+0.19}_{-0.07}$	$-1.36^{+0.43}_{-0.22}$	2.41	4.48

Table 4. The constraints on parameters of Ω_m , h , w_0 and w_a for the flat Λ CDM model, the flat w CDM model, and the CPL model with SNe Ia and GRBs at $z > 1.4$ in the FULL sample, the GOLD sample, and the M2021 sample.

Data Set	Models	Ω_m	h	w_0	w_a	ΔAIC	ΔBIC
GOLD+SNe Ia	Λ CDM	$0.354^{+0.018}_{-0.018}$	$0.7305^{+0.0023}_{-0.0023}$	-	-	0	0
	w CDM	$0.410^{+0.047}_{-0.037}$	$0.7333^{+0.0030}_{-0.0030}$	$-1.22^{+0.18}_{-0.15}$	-	0.28	5.69
	CPL	$0.441^{+0.040}_{-0.032}$	$0.7322^{+0.0032}_{-0.0032}$	$-1.21^{+0.18}_{-0.15}$	$-1.12^{+0.45}_{-0.83}$	0.44	11.25
FULL+SNe Ia	Λ CDM	$0.353^{+0.018}_{-0.018}$	$0.7306^{+0.0023}_{-0.0023}$	-	-	0	0
	w CDM	$0.406^{+0.046}_{-0.036}$	$0.7334^{+0.0031}_{-0.0031}$	$-1.21^{+0.18}_{-0.15}$	-	0.45	5.87
	CPL	$0.435^{+0.039}_{-0.032}$	$0.7319^{+0.0032}_{-0.0032}$	$-1.18^{+0.17}_{-0.13}$	$-1.16^{+0.66}_{-0.80}$	0.69	11.53
M2021+SNe Ia	Λ CDM	$0.340^{+0.018}_{-0.018}$	$0.7319^{+0.0024}_{-0.0024}$	-	-	0	0
	w CDM	$0.348^{+0.064}_{-0.048}$	$0.7323^{+0.0030}_{-0.0030}$	$-1.05^{+0.17}_{-0.14}$	-	1.95	7.35
	CPL	$0.398^{+0.052}_{-0.037}$	$0.7320^{+0.0031}_{-0.0031}$	$-1.08^{+0.17}_{-0.13}$	$-0.96^{+0.58}_{-0.58}$	3.55	14.34

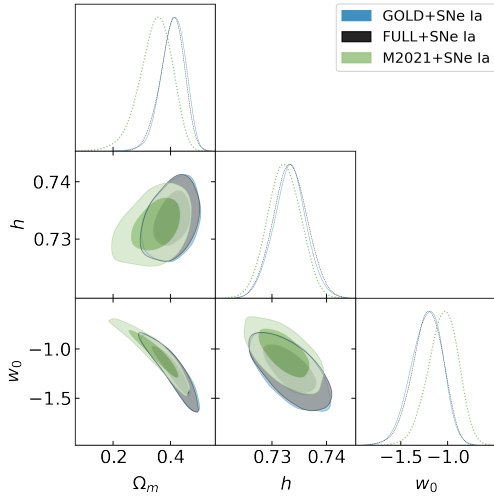


Figure 10. Constraints on parameters of Ω_m , h , and w_0 for the flat w CDM model with SNe Ia and GRBs at $z \geq 1.4$ from the FULL sample (black dashed curves), the GOLD sample (blue curves), and the M2021 sample (green dotted curves) respectively.

relation is slightly favored. Jia et al. (2022) found no statistically significant evidence for the redshift evolution with the Amati relation. However, Frontera et al. (2012) found that the time-resolved relation (the Yonetoku relation: $E_{p,i} - L_{p,iso}$ correlation) is a clear demonstration that the origin of the correlation is physical, and the Amati relation and the Yonetoku relation likely not the result of selection effects. More-

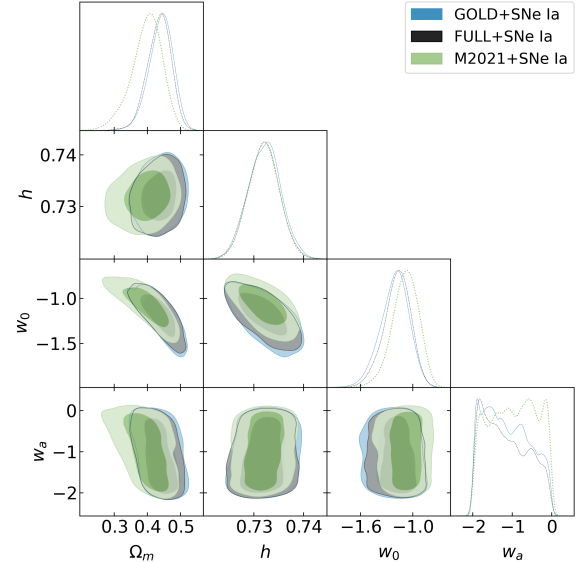


Figure 11. Constraints on parameters of Ω_m , h , w_0 and w_a for the flat CPL model with SNe Ia and GRBs at $z \geq 1.4$ from the FULL sample (black dashed curves), the GOLD sample (blue curves), and the M2021 sample (green dotted curves) respectively.

over, Dainotti & Amati (2018) have given a review of the evidences showing that the Amati relation is NOT affected by relevant selection effects and biases. Further examinations of possible evolutionary effects should be required for considering GRBs as standard candles for a cosmological probe.

For the GRB satellites, the Konus-Wind (KW) experiment plays an important role in GRB studies thanks to its unique set of characteristics: the spacecraft orbit in interplanetary space that provides an exceptionally stable background; the continuous coverage of the full sky by two omnidirectional detectors; and the broad energy range (20 keV-15MeV, triggered mode) since 1994. The *Swift* satellite was launched in 2004, with the Burst Alert Telescope (BAT) instrument which is capable of detecting energies up to 150 keV (Gehrels et al. 2004). In the future, we are looking forward to the observations by the French-Chinese satellite spacebased multi-band astronomical variable objects monitor (SVOM) (Wei et al. 2016) and the Transient High-Energy Sky and Early Universe Surveyor (THESEUS) (Amati et al. 2018).

Attea et al. (2017) used the sample of GRBs with redshift detected by Fermi/GBM (52 GRBs with a cutoff at GRB160629) and KW to investigate the maximum isotropic energy of GRBs; Tsvetkova et al. (2021) presented a systematic study of GRBs with reliable redshift estimates detected simultaneously by the KW and the Swift/BAT during 2005-2018. Oates (2023) provided an overview of the long GRBs observed by the Ultra-Violet/Optical Telescope (UVOT) on-board *Swift*, and review the major discoveries that have been achieved by the *Swift*/UVOT over the last 18 years during 2004-2022. Along with the GRB sample from KW, Swift, and Fermi, as well as SVOM and THESEUS, GRBs could be used as an additional choice to help us explore universe using GRBs at high-redshift.

ACKNOWLEDGMENTS

We are grateful to Dr. Ariadna Montiel, Prof. Øyvind Grøn for useful discussions. We also thank the referee for helpful comments and constructive suggestions. This project was supported by the Guizhou Provincial Science and Technology Foundations (QKHJC-ZK[2021] Key 020 and QKHJC-ZK[2024] general 443).

DATA AVAILABILITY

Data are available at the following references: the Fermi GRB sample are from this work and references therein, the Pantheon+ SNe Ia sample from Scolnic et al. (2022), and the latest OHD obtained with the CC method from Moresco et al. (2020, 2022) and Li, Zhang & Liang (2023).

REFERENCES

- Akritas M. G., & Bershadsky M. A. 1996, *ApJ*, 470, 706
 Amati L. 2006, *MNRAS*, 372, 233
 Amati L., Frontera, F., & Guidorzi, C. 2009, *A&A*, 508, 173
 Amati L., & Valle M. D. 2013, *IJMPD*, 22, 1330028
 Amati L., Frontera F., Tavani M., et al., 2002, *A&A*, 390, 81
 Amati, Guidorzi, Frontera, et al., 2008, *MNRAS*, 391, 577
 Amati L., Della Valle M., 2013, *IJMPD*, 22, 1330028
 Amati L., O'Brien P., Gotz D., et al., 2018, *AdSpR*, 62, 191
 Amati L., D'Agostino R., Luongo O., et al. 2019, *MNRAS*, 486, L46
 Attea J.-L., Heussaff, V., Dezalay, J.-P. et al., 2017, *ApJ*, 837, 119
 Band D., Matteson J., Ford L., et al., 1993, *ApJ*, 280, 872
 Bernardini M. G., Margutti R., Zaninoni E., & Chincarini G. 2012, *MNRAS*, 425, 1199
 Narayana Bhat P., Meegan C. A., von Kienlin A., et al., 2016, *ApJS*, 223, 28
 Brout D., et al., 2022, *ApJ*, 938, 110
 Butler N. R., Kocevski D., Bloom J. S., Curtis J. L., 2007, *ApJ*, 671, 656
 Butler N. R., Kocevski D., Bloom J. S., 2009, *ApJ*, 694, 76
 Butler N. R., Bloom J. S., Poznanski D., 2010, *ApJ*, 711, 495
 Chevallier, M. & Polarski, D. 2001, *IJMPD*, 10, 213
 Cucchiara, A., Levan, A., Fox, D. B., et al., 2011, *ApJ*, 736, 7
 Cunningham V., & SEDM Team, 2019, *GCN*, 24835
 D'Agostini G. 2005, *arXiv: physics/0511182*
 Dai, Z., Liang, E., & Xu, D. 2004, *ApJ*, 612, L101
 Dainotti M. G., & Amati L. 2018, *PASP*, 130, 051001
 Dainotti M., & Del Vecchio R. 2017, *New Astronomy Reviews*, 77, 23
 Dainotti M. G., Cardone V. F., & Capozziello S. 2008, *MNRAS*, 391, L79
 Dainotti M. G., Ostrowski M., & Willingale R. 2011, *MNRAS*, 418, 2202
 Dainotti M. G., Nagataki S., Maeda K., et al., 2017, *A&A*, 600, A98
 Dainotti M. G., Levine D., Fraija N., et al., 2023, *Galaxies*, 11, 25
 Demianski M., Piedipalumbo E., Sawant D., et al., 2017, *A&A*, 598, A112
 Demianski M., Piedipalumbo E., Sawant D., et al., 2017, *A&A*, 598, A113
 Fana Dirirsa F., Razzaque S., Piron F., et al., 2019, *ApJ*, 887, 13
 Fenimore E. E., & Ramirez-Ruiz E. *arXiv: astro-ph/0004176*
 Foreman-Mackey D., Conley A., Meierjürgen Farr W., et al., 2015, 306
 Frontera F., Amati L., Guidorzi C., et al., 2012, *ApJ*, 754, 138
 Ghirlanda G., Ghisellini G., & Lazzati D. 2004, *ApJ*, 616, 331
 Ghirlanda, G., Ghisellini, G., & Firmani, C. 2006, *New, J. Phys.*, 8, 123
 Ghirlanda G., Nava L., Ghisellini G., et al., 2007, *A&A*, 466, 127
 Goldstein A., Veres P., Burns E., Briggs M. S., et al., 2017, *ApJ*, 848, L14
 Gehrels N., Chincarini G., Giommi P., et al., 2004, *ApJ*, 611, 1005
 Ghirlanda G., Nava L., Ghisellini G., et al., 2008, *MNRAS*, 387, 319
 Goldstein A., Burgess J. M., Preece R. D., et al., 2012, *ApJS*, 199, 19
 Gruber D., Goldstein A., Weller von Ahlefeld V., et al., 2014, *ApJS*, 211, 12
 Hogg D. W., Bovy J., & Lang D., 2010, *arXiv*, arXiv:1008.4686.
 Heintz, K. E., Fynbo J. P. U., de Ugarte Postigo A., 2019, *GCN*, 24686
 Higgins, A. B., van der Horst, A. J., Starling, R. L. C. et al. 2019, *MNRAS*, 484, 5245
 Iyyani, S., Ryde F., Axelsson, M., et al., 2013, *MNRAS*, 433, 2739
 Izzo, L., Muccino, M., Zaninoni, E., Amati L., et al., 2015, *A & A*, 582, A115
 Jia X. D., Hu J. P., Yang J., Zhang B. B., Wang F. Y. 2022, *MNRAS*, 516, 2575
 Jordana-Mitjans N., Mundell C. G., Guidorzi C., et al., 2022, *ApJ*, 939, 106
 Khadka, N. & Ratra, B. 2020, *MNRAS*, 499, 391
 Khadka, N., Luongo, O., Muccino, M., & Ratra, B. 2021, *JCAP*, 09, 042
 Li Z., Zhang B., Liang N. 2023, *MNRAS*, 521, 4406
 Liang E., Zhang B. 2005, *ApJ*, 633, 611
 Liang, E., & Zhang, B. 2006, *MNRAS*, 369, L37
 Liang N., Xiao W. K., Liu Y. 2008, *ApJ*, 685, 354
 Li, Z., Zhang, B., & Liang, N. 2023, *MNRAS*, 521, 4406
 Li, J.-L., Yang, Y.-P., Yi, S.-X., Hu, J.-P., Wang, F.-Y., & Qu, Y.-K. 2023, *ApJ*, 953, 58

- Liang, N., Xiao, W. K., Liu, Y., & Zhang, S. N. 2008, *ApJ*, 685, 354
- Liang, N., & Zhang, S. 2008, *AIP Conf. Proc. Vol. 1065, Am. Inst. Phys New York*
- Liang, N., Wu, P., & Zhang, S. N. 2010, *PRD*, 81, 083518
- Liang, N., Xu, L., & Zhu, Z. H. 2011, *A&A*, 527, A11
- Liang, N., Li, Z., Xie, X., & Wu, P. 2022, *ApJ*, 941, 84
- Linder, E.V. 2003, *PRL*, 90, 091301
- Lin H.-N., Li X., Chang Z. 2015, *MNRAS*, 455, 2131
- Liu, J., & Wei, H. 2015, *GRGr*, 47, 141
- Liu, Y., Chen, F., Liang, N., et al. 2022, *ApJ*, 931, 50
- Liu, Y., Liang, N., Xie, X., et al. 2022, *ApJ*, 935, 7
- Luongo O., Muccino M. 2021a, *Galaxy*, 9, 77
- Luongo, O., & Muccino, M. 2021b, *MNRAS*, 503, 4581
- Luongo, O., & Muccino, M. 2023, *MNRAS*, 518, 2247
- Lusso E., Piedipalumbo E., Risaliti G., & Paolillo M. 2019, *A & A*, 628, L4
- Margutti R., Zaninoni E., Bernardini M. G., et al., 2012, *MNRAS*, 428, 729
- Meegan C., Lichti G., Bhat P. N., et al., 2009, *ApJ*, 702, 791
- Montiel, A., Cabrera, J. I., & Hidalgo, J. C. 2021, *MNRAS*, 501, 3515
- Moresco, M., Verde, L., Pozzetti, L., Jimenez, R. & Cimatti, A. 2012, *JCAP*, 08, 006
- Moresco, M. 2015, *MNRAS*, 450, L16
- Moresco, M., Pozzetti, L., Cimatti, A. et al. 2016, *JCAP*, 05, 014
- Moresco M., Jimenez R., Verde L., et al. 2020, *ApJ*, 898, 82
- Moresco M., Amati L., Amendola L., et al., 2022, *LRR*, 25, 1
- Nava L., Salvaterra R., Ghirlanda G., et al., 2012, *MNRAS*, 421, 1256
- Nemmen R. S., Georganopoulos M., Guiriec S., et al, 2012, *Science*, 338, 1445
- Norris J. P., Marani G. F., & Bonnell J. T. 2000, *ApJ*, 534, 248
- Oates, S. *Universe* 2023, 9(3), 113; doi:10.3390/universe9030113
- Oates, S., 2023, *Universe*, 9(3), 113
- Paciesas W. S., Meegan C. A., von Kienlin A., et al., 2012, *ApJS*, 199, 18
- Perley D. A., Schulze S., de Ugarte Postigo A., et al., 2016, *ApJ*, 817, 7
- Phillips M. M. et al. 1993, *ApJ*, 413, L105
- Planck Collaboration, Aghanim N., Akrami Y., et al., 2020, *A&A*, 641, A1
- Poolakkil S., Preece R., Fletcher C., et al., 2021, *ApJ*, 913, 60
- Reichart D. E. *arXiv: astro-ph/9912368*
- Riess, A.G., et al, 2022, *ApJ*, 938, 36
- Salvaterra R., Della Valle M., Campana S., et al., 2009, *Nature*, 461, 1258
- Schaefer, B. E. 2003, *ApJ*, 583, L67
- Schaefer, B. E. 2007, *ApJ*, 660, 16
- Schroeder, G., Laskar, T., Fong, W. et al. 2022, *ApJ*, 940, 53
- Scolnic, D. M., Jones, D. O., Rest, A., et al., 2018, *ApJ*, 859, 101
- Scolnic D., Brout D., Carr A., et al., 2022, *ApJ*, 938, 113
- Seikel M., Clarkson C., & Smith M. 2012, *JCAP*, 06, 036
- Tanvir N. R., Fox D. B., Levan A. J., et al., 2009, *Nature*, 461, 1254
- Tang C. H., Huang Y. F., Geng J. J., & Zhang Z. B. 2019, *ApJS*, 245, 1
- Tang L., Li X., Lin, H.-N., & Liu L. 2021, *ApJ*, 907, 121
- Tsvetkova A., Frederiks D., Svinkin, D. et al., 2021, *ApJ*, 908, 83
- von Kienlin A., Meegan C. A., Paciasas W. S., et al., 2014, *ApJS*, 211, 13
- von Kienlin A., Meegan C. A., Paciasas W. S., et al., 2020, *ApJ*, 893, 46
- Wang, F., & Dai, Z. G. 2006, *MNRAS*, 368, 371
- Wang, J. S., Wang, F. Y., Cheng, K. S., & Dai, Z. G. 2016, *AA*, 585, A68
- Wang, G.Z., Li, X. L. & Liang, N. *arXiv:2404.14237*
- Wei J., Cordier B., Antier S., et al., 2016, *arXiv:1610.06892*
- Wei, H., & Zhang, S. N. 2009, *EPJ C*, 63, 139
- Wei, H., 2010, *JCAP*, 08, 020
- Xie, H., Nong, X., Wang, H., Zhang, B., Li, Z. & Liang, N. *arXiv:2307.16467*
- Yonetoku D., Murakami T., Nakamura T., et al., 2004, *ApJ*, 609, 935
- Zhang, B., Xie, X., Nong, X., Wang, H., Li, Z. & Liang, N. *arXiv:2312.09440*
- Zhang X.-L., Huang Y.-F., Zou Z.-C., 2023, *RAA*, 23, 125003

This paper has been typeset from a $\text{T}_{\text{E}}\text{X}/\text{L}^{\text{A}}\text{T}_{\text{E}}\text{X}$ file prepared by the author.

APPENDIX A: DATA SAMPLE TABLE

Table A1: The GOLD sample (123 LGRBs) table.

GRB	z	T_{90}	α	σ_α	β	σ_β	$E_{p,i}$ (keV)	$\sigma_{E_{p,i}}$ (keV)	S_{bolo} (erg/cm ²)	$\sigma_{S_{\text{bolo}}}$ (erg/cm ²)
080804	2.2045	24.7	-5.175E-01	7.985E-02	-1.905E+00	8.533E-02	7.088E+02	7.356E+01	1.357E-05	6.537E-07
080810	3.35	75.2	-1.090E+00	4.453E-02	-5.982E+00	9.814E+01	2.564E+03	3.734E+02	1.165E-05	4.552E-07
080916A	0.689	46.34	-7.807E-01	1.063E-01	-1.774E+00	4.619E-02	1.786E+02	3.454E+01	1.473E-05	7.589E-07
081121	2.512	41.99	-4.351E-01	1.148E-01	-2.096E+00	9.481E-02	5.652E+02	5.074E+01	1.985E-05	8.038E-07
081221	2.26	29.7	-8.387E-01	2.245E-02	-3.675E+00	4.704E-01	2.833E+02	4.328E+00	3.286E-05	2.109E-07
081222	2.77	18.88	-8.444E-01	4.478E-02	-2.300E+00	1.188E-01	5.550E+02	3.179E+01	1.434E-05	4.283E-07
090113	1.7493	17.41	-1.183E+00	1.420E-01	-2.065E+00	5.152E-01	3.922E+02	8.461E+01	2.194E-06	4.937E-07
090323	3.57	133.9	-1.183E+00	1.145E-02	-2.354E+00	1.470E-01	2.073E+03	1.078E+02	1.364E-04	2.690E-06
090328A	0.736	61.7	-1.083E+00	1.657E-02	-2.390E+00	2.323E-01	1.129E+03	7.598E+01	6.532E-05	4.546E-06
090424	0.544	14.14	-1.022E+00	1.625E-02	-2.763E+00	1.704E-01	2.470E+02	6.140E+00	5.427E-05	1.593E-06
090516A	4.109	123.1	-1.456E+00	4.396E-02	-2.460E+00	8.406E-01	7.563E+02	1.012E+02	2.068E-05	1.338E-06
090618	0.54	112.4	-1.114E+00	1.308E-02	-2.239E+00	2.007E-02	2.295E+02	5.061E+00	3.698E-04	3.627E-06
090902B	1.822	19.33	-1.008E+00	4.173E-03	-9.722E+00	4.105E+02	2.978E+03	4.590E+01	3.547E-04	2.618E-06
090926A	2.1062	13.76	-8.480E-01	8.619E-03	-2.378E+00	4.558E-02	1.037E+03	1.814E+01	1.887E-04	2.308E-06
090926B	1.24	64	2.346E-01	1.057E-01	-3.343E+00	4.482E-01	1.844E+02	5.736E+00	1.087E-05	1.754E-07
091003A	0.8969	20.22	-1.072E+00	2.277E-02	-2.215E+00	1.480E-01	7.023E+02	5.047E+01	3.435E-05	2.238E-06
091020	1.71	24.26	-1.245E+00	8.075E-02	-2.454E+00	3.775E+01	6.188E+02	1.323E+02	1.058E-05	8.474E-05
091024	1.092	93.95	-1.329E+00	8.007E-02	-6.127E+00	2.440E+02	3.758E+03	1.932E+03	1.653E-05	2.810E-06
091127	0.49	8.701	-1.254E+00	6.618E-02	-2.216E+00	2.009E-02	5.283E+01	2.310E+00	3.034E-05	4.794E-07
091208B	1.063	12.48	-6.152E-01	2.236E-01	-1.923E+00	4.911E-02	9.227E+01	2.631E+01	9.474E-06	4.674E-07
100414A	1.368	26.5	-6.242E-01	1.384E-02	-3.534E+00	1.245E+00	1.571E+03	3.639E+01	1.176E-04	8.121E-06
100615A	1.398	37.38	-9.064E-01	1.560E-01	-1.803E+00	3.070E-02	1.284E+02	1.800E+01	1.431E-05	3.925E-07
100728A	1.567	165.4	-5.097E-01	2.151E-02	-2.542E+00	9.954E-02	6.518E+02	1.686E+01	1.564E-04	4.154E-06
100814A	1.44	150.5	-2.419E-01	1.001E-01	-2.437E+00	2.555E-01	3.116E+02	2.130E+01	1.775E-05	1.387E-06
100816A	0.8035	2.045	-3.178E-01	7.378E-02	-2.733E+00	2.726E-01	2.401E+02	1.277E+01	4.101E-06	2.296E-07
100906A	1.727	110.6	-9.263E-01	2.344E-01	-1.861E+00	1.001E-01	2.043E+02	6.617E+01	3.543E-05	2.381E-06
101213A	0.414	45.06	-9.755E-01	6.427E-02	-2.374E+00	7.771E-01	4.931E+02	4.786E+01	1.049E-05	3.411E-06
110213A	1.46	34.31	-1.563E+00	4.812E-02	-4.870E+00	0.000E+00	2.769E+02	2.961E+01	1.207E-05	3.160E-07
110402A	0.854	35.65	-1.352E+00	7.834E-02	-9.306E+00	1.427E+04	1.865E+03	9.950E+02	1.718E-05	3.393E-06
110731A	2.83	7.485	-8.686E-01	3.117E-02	-2.436E+00	2.741E-01	1.234E+03	6.479E+01	8.812E-05	1.502E-06
111228A	0.714	99.84	-1.584E+00	8.630E-02	-2.446E+00	8.507E-02	4.550E+01	2.343E+00	2.931E-05	9.430E-07
120119A	1.728	55.3	-9.550E-01	3.240E-02	-2.366E+00	1.603E-01	4.986E+02	2.851E+01	4.823E-05	2.189E-06
120326A	1.798	11.78	-6.790E-01	2.284E-01	-2.335E+00	1.347E-01	1.240E+02	1.563E+01	4.005E-06	1.666E-07
120624B	2.1974	271.4	-9.157E-01	1.224E-02	-2.216E+00	7.805E-02	2.032E+03	7.402E+01	2.824E-04	5.881E-06
120711A	1.405	44.03	-9.844E-01	8.513E-03	-2.796E+00	9.103E-02	3.169E+03	1.016E+02	3.606E-04	5.699E-06
120712A	4.1745	22.53	6.105E+00	6.714E-01	-1.608E+00	3.826E-02	1.758E+02	1.996E+01	6.096E-06	1.320E-07
120716A	2.486	226	-8.946E-01	5.233E-02	-2.630E+00	2.198E-01	4.180E+02	2.252E+01	1.447E-05	4.231E-07
120811C	2.671	14.34	-7.028E-01	2.255E-01	-2.839E+00	3.367E-01	2.034E+02	1.443E+01	3.917E-06	2.737E-07
120907A	0.97	5.76	-8.553E-01	2.148E-01	-4.902E+00	5.076E+01	2.527E+02	5.961E+01	8.580E-07	1.440E-07
120909A	3.93	112.1	-8.436E-01	5.132E-02	-1.934E+00	7.372E-02	9.843E+02	1.197E+02	1.260E-05	3.443E-07
121128A	2.2	17.34	-6.837E-01	1.195E-01	-2.424E+00	9.205E-02	1.923E+02	1.232E+01	1.096E-05	2.588E-07
130215A	0.597	143.7	-1.059E+00	9.077E-02	-1.615E+00	4.154E-02	3.353E+02	6.757E+01	4.402E-05	2.468E-06
130420A	1.297	105	-9.366E-01	1.738E-01	-2.921E+00	4.152E-01	1.212E+02	8.541E+00	1.376E-05	5.858E-07
130427A	0.3399	138.2	-1.018E+00	1.843E-03	-2.829E+00	3.238E-02	1.105E+03	7.299E+00	3.912E-03	2.169E-05
130518A	2.488	48.58	-8.629E-01	1.561E-02	-2.181E+00	6.691E-02	1.329E+03	5.082E+01	1.280E-04	2.619E-06
130610A	2.092	21.76	-1.595E+00	7.599E-02	-1.863E+01	2.230E+10	9.460E+02	4.954E+02	4.627E-06	3.145E-07
130702A	0.145	58.88	-1.736E-01	1.458E+01	-2.453E+00	3.650E-02	1.110E+01	8.544E+00	9.512E-06	1.256E-05
130925A	0.347	215.6	-1.106E-01	1.831E-01	-2.006E+00	3.260E-02	3.120E+01	1.089E+00	1.302E-04	3.620E-06
131011A	1.874	77.06	-8.778E-01	7.417E-02	-2.085E+00	2.288E-01	6.255E+02	1.175E+02	1.227E-05	1.247E-06
131105A	1.686	112.6	-1.263E+00	2.244E-02	-9.128E+00	5.123E+03	7.218E+02	4.918E+01	2.663E-05	2.127E-06
131108A	2.4	18.18	-9.140E-01	1.993E-02	-2.464E+00	1.859E-01	1.247E+03	5.540E+01	4.496E-05	1.721E-06
131231A	0.642	31.23	-1.218E+00	9.639E-03	-2.305E+00	3.373E-02	2.924E+02	6.619E+00	2.059E-04	2.734E-06
140206A	2.73	27.26	5.490E-02	9.329E-02	-2.416E+00	9.637E-02	4.521E+02	2.173E+01	1.780E-05	4.141E-07
140213A	1.2076	18.62	-1.126E+00	3.499E-02	-2.252E+00	5.515E-02	1.902E+02	9.051E+00	2.799E-05	5.511E-07
140423A	3.26	95.23	-5.542E-01	1.155E-01	-1.786E+00	4.965E-02	4.949E+02	6.768E+01	2.514E-05	6.316E-07
140506A	0.889	64.13	-1.180E+00	1.065E-01	-1.682E+01	5.176E+07	3.715E+02	4.779E+01	7.174E-06	2.228E-06
140508A	1.027	44.29	-1.182E+00	1.890E-02	-2.319E+00	9.382E-02	5.218E+02	2.457E+01	8.302E-05	2.704E-06
140512A	0.725	148	-1.225E+00	1.754E-02	-3.540E+00	1.616E+01	1.192E+03	1.005E+02	4.073E-05	2.049E-05
140606B	0.384	22.78	-1.239E+00	4.621E-02	-2.037E+00	4.716E-01	7.387E+02	1.561E+02	1.347E-05	3.904E-06
140620A	2.04	45.83	-8.497E-01	1.905E-01	-2.092E+00	8.071E-02	2.112E+02	3.260E+01	8.075E-06	2.972E-07
140703A	3.14	83.97	-1.267E+00	5.914E-02	-2.681E+00	9.169E-01	8.647E+02	1.438E+02	9.012E-06	7.920E-07
140801A	1.32	7.168	-3.846E-01	3.932E-02	-3.853E+00	1.200E+00	2.770E+02	6.121E+00	1.279E-05	2.520E-07
140808A	3.29	4.477	-4.223E-01	1.004E-01	-2.868E+00	4.827E-01	5.039E+02	2.771E+01	3.445E-06	1.376E-07
140907A	1.21	35.84	-1.018E+00	5.045E-02	-1.373E+01	1.080E+06	3.082E+02	2.279E+01	6.932E-06	1.984E-06
141004A	0.573	2.56	5.630E-02	5.375E-01	-1.891E+00	7.405E-02	4.375E+01	1.045E+01	1.933E-06	1.533E-07
141028A	2.33	31.49	-8.420E-01	2.806E-02	-1.966E+00	5.182E-02	9.760E+02	5.988E+01	5.019E-05	1.185E-06
141220A	1.3195	7.616	-8.324E-01	4.552E-02	-1.027E+01	1.171E+04	4.153E+02	2.335E+01	5.550E-06	1.126E-06

The GOLD sample (123 LGRBs) table. (continued)

GRB	z	T_{90}	α	σ_α	β	σ_β	$E_{p,i}$ (keV)	$\sigma_{E_{p,i}}$ (keV)	S_{bolo} (erg/cm ²)	$\sigma_{S_{\text{bolo}}}$ (erg/cm ²)
141221A	1.452	23.81	-8.051E-01	2.786E-01	-1.970E+00	2.347E-01	2.259E+02	7.044E+01	5.903E-06	8.685E-07
141225A	0.915	56.32	-2.982E-01	1.555E-01	-2.059E+00	1.662E-01	3.415E+02	3.693E+01	5.638E-06	6.387E-07
150301B	1.5169	13.31	-1.049E+00	9.013E-02	-2.222E+00	4.398E-01	4.606E+02	7.213E+01	4.089E-06	6.709E-07
150314A	1.758	10.69	-6.792E-01	1.382E-02	-2.601E+00	1.021E-01	9.575E+02	2.178E+01	1.017E-04	2.333E-06
150403A	2.06	22.27	-8.733E-01	1.830E-02	-2.108E+00	5.752E-02	1.312E+03	6.443E+01	7.922E-05	1.738E-06
150514A	0.807	10.81	-1.206E+00	9.780E-02	-2.431E+00	1.824E-01	1.167E+02	1.067E+01	6.148E-06	2.786E-07
150727A	0.313	49.41	1.314E-01	2.777E-01	-2.158E+00	1.985E-01	1.947E+02	2.398E+01	6.557E-06	9.681E-07
150821A	0.755	103.4	-1.244E+00	1.676E-02	-2.131E+00	9.393E-02	4.935E+02	3.002E+01	7.832E-05	3.769E-06
151027A	0.81	123.4	-1.247E+00	4.736E-02	-1.955E+00	9.463E-02	3.645E+02	4.430E+01	2.287E-05	1.519E-06
160509A	1.17	369.7	-1.015E+00	9.913E-03	-2.232E+00	4.756E-02	7.708E+02	2.143E+01	2.557E-04	4.928E-06
160625B	1.406	453.4	-9.341E-01	4.352E-03	-2.182E+00	2.018E-02	1.134E+03	1.551E+01	9.629E-04	7.812E-06
160629A	3.332	64.77	-1.016E+00	3.634E-02	-2.652E+00	1.504E+00	1.202E+03	9.250E+01	1.530E-05	2.664E-06
160804A	0.736	131.6	-1.030E+00	8.786E-02	-2.819E+00	9.034E-01	1.239E+02	7.249E+00	1.907E-05	1.525E-06
161014A	2.823	36.61	-7.569E-01	8.587E-02	-1.919E+01	4.129E+08	6.462E+02	5.513E+01	6.313E-06	6.033E-07
161017A	2.0127	37.89	-1.030E+00	1.010E-01	-2.371E+00	7.765E-01	7.188E+02	1.228E+02	6.120E-06	1.209E-06
161117A	1.549	122.2	-8.111E-01	5.158E-02	-3.023E+00	5.141E-01	2.056E+02	7.762E+00	3.479E-05	9.663E-07
161129A	0.645	36.1	-1.037E+00	9.784E-02	-1.954E+00	1.622E-01	2.408E+02	7.009E+01	1.064E-05	1.388E-06
170214A	2.53	122.9	-9.788E-01	8.669E-03	-2.512E+00	1.021E-01	1.699E+03	3.963E+01	2.283E-04	3.879E-06
170405A	3.51	78.59	-7.993E-01	1.996E-02	-2.354E+00	8.888E-02	1.204E+03	4.189E+01	8.858E-05	1.487E-06
170607A	0.557	20.93	-1.286E+00	5.950E-02	-2.383E+00	0.000E+00	1.741E+02	1.406E+01	1.243E-05	1.587E-07
170705A	2.01	22.78	-9.911E-01	6.923E-02	-2.303E+00	1.083E-01	2.946E+02	2.301E+01	1.661E-05	4.933E-07
170728B	1.272	46.34	-9.615E-01	1.287E-01	-2.436E+00	3.052E+00	3.101E+02	6.521E+01	4.927E-06	4.034E-06
170903A	0.886	25.6	-1.312E+00	1.088E-01	-2.434E+01	7.713E+11	1.793E+02	2.525E+01	4.096E-06	4.273E-06
171010A	0.33	107.3	-1.089E+00	5.936E-03	-2.191E+00	8.671E-03	1.831E+02	1.898E+00	9.013E-04	4.507E-06
180205A	1.409	15.36	-7.653E-01	7.705E-01	-2.130E+00	1.681E-01	8.480E+01	4.100E+01	2.790E-06	3.265E-07
180314A	1.445	22.02	-4.038E-01	7.725E-02	-3.356E+00	1.473E+00	2.517E+02	1.097E+01	1.399E-05	7.652E-07
180620B	1.1175	46.72	-1.206E+00	1.156E-01	-1.660E+00	3.474E-02	3.719E+02	1.054E+02	1.809E-05	6.632E-07
180703A	0.6678	20.74	-7.756E-01	4.122E-02	-1.967E+00	1.032E-01	5.850E+02	5.378E+01	2.873E-05	2.242E-06
180720B	0.654	48.9	-1.171E+00	4.805E-03	-2.490E+00	7.095E-02	1.052E+03	2.551E+01	4.490E-04	8.034E-06
180728A ^a	0.117	6.4	-1.540E+00	1.000E-02	-2.460E+00	2.000E-02	8.847E+01	1.564E+00	7.835E-05	4.395E-07
181020A ^a	2.938	15.1	-7.000E-01	2.000E-02	-2.060E+00	7.000E-02	1.445E+03	6.695E+01	3.840E-05	8.864E-07
190114C ^a	0.425	116.4	-1.058E+00	3.000E-03	-3.180E+00	7.000E-02	1.423E+03	1.696E+01	7.371E-04	5.482E-06
190324A ^a	1.1715	26.88	-8.400E-01	4.000E-02	-2.060E+00	5.000E-02	3.133E+02	1.824E+01	2.348E-05	7.454E-07
190719C ^b	2.469	175.6	-8.600E-01	2.100E-01	-2.740E+00	5.800E-01	2.780E+02	4.059E+01	8.098E-06	4.550E-07
190829A ^a	0.0785	59.39	-9.200E-01	6.200E-01	-2.510E+00	1.000E-02	1.186E+01	1.079E+00	2.681E-05	2.428E-06
200524A ^a	1.256	37.76	-6.600E-01	6.000E-02	-1.770E+00	3.000E-02	4.332E+02	3.610E+01	2.502E-05	6.818E-07
200613A ^a	1.228	478	-1.080E+00	2.000E-02	-2.580E+00	8.000E-02	2.473E+02	6.684E+00	5.873E-05	8.958E-07
201020B ^a	0.804	15.87	-7.100E-01	2.000E-02	-2.200E+00	3.000E-02	2.470E+02	6.134E+00	4.630E-05	7.386E-07
201216C ^a	1.1	29.95	-1.060E+00	1.000E-02	-2.250E+00	3.000E-02	6.846E+02	1.470E+01	1.921E-04	2.315E-06
210104A ^b	0.46	31.75	-1.101E+00	7.550E-02	-2.449E+00	4.020E-01	2.808E+02	3.913E+01	2.467E-05	3.315E-06
210204A ^a	0.876	206.9	-1.500E+00	1.000E-01	-2.300E+00	5.000E-01	2.626E+02	9.380E+01	1.068E-04	1.592E-05
210610A ^b	3.54	8.192	-4.720E-01	5.670E-01	-1.983E+00	1.770E-01	3.154E+02	1.130E+02	1.604E-06	1.124E-07
210610B ^b	1.13	55.04	-3.700E-01	2.000E-02	-3.080E+00	2.300E-01	7.977E+02	1.815E+01	1.302E-04	4.531E-06
210619B ^a	1.937	54.79	-8.600E-01	1.000E-02	-1.990E+00	1.000E-02	6.168E+02	8.811E+00	4.341E-04	2.213E-06
210722A ^b	1.145	61.95	-8.770E-01	2.830E-01	-3.407E+00	5.420E+00	2.390E+02	6.435E+01	4.756E-06	8.564E-07
210731A ^b	1.2525	25.86	5.000E-02	1.900E-01	-3.300E+00	1.170E+00	4.343E+02	4.009E+01	3.236E-06	3.190E-07
211023A ^a	0.39	79.11	-1.740E+00	1.000E-02	-2.550E+00	7.000E-02	1.279E+02	2.780E+00	1.367E-04	1.530E-06
220101A ^a	4.618	128.3	-1.060E+00	2.000E-02	-2.300E+00	2.000E-01	1.629E+03	1.011E+02	7.116E-05	1.810E-06
220107A ^a	1.246	33.03	-5.500E-01	6.000E-02	-1.940E+00	6.000E-02	3.773E+02	2.471E+01	2.811E-05	1.202E-06
220521A ^b	5.6	13.57	-1.600E-01	7.900E-01	-2.910E+00	6.600E-01	3.410E+02	6.600E+01	9.846E-07	6.278E-08
220527A ^a	0.857	10.5	-7.500E-01	2.000E-02	-2.550E+00	5.000E-02	2.815E+02	5.014E+00	6.180E-05	8.231E-07
220627A ^a	3.084	136.7	-8.100E-01	3.000E-02	-2.680E+00	3.100E-01	1.593E+03	8.168E+01	5.431E-05	2.216E-06
221226B ^b	2.694	4.864	2.600E-01	3.100E-01	-5.180E+00	1.580E+01	3.794E+02	3.642E+01	1.153E-06	2.311E-08
230204B ^a	2.142	216.1	-9.700E-01	2.000E-02	-2.730E+00	2.900E-01	2.397E+03	1.414E+02	1.020E-04	3.063E-06
230812B ^a	0.36	3.264	-8.000E-01	1.000E-02	-2.470E+00	2.000E-02	3.713E+02	4.080E+00	3.702E-04	2.923E-06
230818A ^b	2.42	9.981	-8.000E-01	7.000E-02	-2.510E+00	4.500E-01	7.312E+02	8.926E+01	4.387E-06	3.846E-07

^a The spectral parameters of 18 GRBs are taken from the GCN.

^b The spectral parameters of 9 GRBs are obtained in this work.

Table A2: The 28 LGRB data in the FULL sample which are not in the GOLD sample.

GRB	z	T_{90}	α	σ_α	β	σ_β	$E_{p,i}$ (keV)	$\sigma_{E_{p,i}}$ (keV)	S_{bolo} (erg/cm ²)	$\sigma_{S_{\text{bolo}}}$ (erg/cm ²)
080905B	2.374	106	-8.523E-01	1.736E-01	-2.316E+00	1.645E+01	6.160E+02	1.739E+02	3.578E-06	1.564E-05
080916C	4.35	62.98	-1.070E+00	1.449E-02	-2.152E+00	7.649E-02	3.572E+03	2.230E+02	7.770E-05	8.500E-07
081109A	0.9787	58.37	-1.899E-01	2.731E-01	-1.649E+00	5.174E-02	5.661E+01	2.173E+01	1.314E-05	8.112E-07
090423	8.2	7.168	-5.529E-01	3.648E-01	-2.620E+00	1.287E+00	6.097E+02	9.979E+01	8.734E-07	8.334E-08
101219B	0.5519	51.01	8.853E-01	4.932E-01	-2.391E+00	2.761E-01	9.825E+01	2.501E+01	4.734E-06	5.468E-07
110106B	0.618	35.52	-9.437E-01	1.370E-01	-8.148E+00	3.141E+03	2.121E+02	2.408E+01	4.385E-06	1.891E-06
110818A	3.36	67.07	-1.054E+00	1.357E-01	-1.805E+00	1.686E-01	8.056E+02	2.223E+02	7.186E-06	5.006E-07
111107A	2.893	12.03	-1.252E+00	1.739E-01	-2.000E+00	0.000E+00	8.326E+02	3.781E+02	1.233E-06	5.329E-08
120118B	2.943	37.83	-2.970E-01	2.542E-01	-2.547E+00	1.492E-01	1.698E+02	1.206E+01	3.020E-06	9.164E-08
120922A	3.1	182.3	-5.366E-01	1.096E+00	-2.228E+00	7.979E-01	1.476E+02	1.665E+01	1.002E-05	1.723E-06
121211A	1.023	5.632	-2.936E-01	2.445E-01	-4.900E+00	1.867E+01	2.048E+02	2.803E+01	6.602E-07	4.518E-08
130612A	2.006	7.424	3.295E-01	5.639E-01	-2.254E+00	1.824E-01	8.699E+01	2.475E+01	8.187E-07	8.919E-08
131229A	1.04	12.99	-7.258E-01	2.305E-02	-4.309E+00	3.085E+00	7.728E+02	2.710E+01	2.890E-05	2.238E-06
140304A	5.283	31.23	-7.893E-01	1.765E-01	-2.429E+00	6.779E-01	7.692E+02	1.975E+02	2.691E-06	1.640E-07
140623A	1.92	111.1	-1.422E+00	9.893E-02	-1.630E+01	1.163E+08	9.535E+02	4.037E+02	3.873E-06	2.532E-07
140713A	0.935	5.376	2.956E-01	7.273E-01	-1.806E+00	1.272E-01	7.130E+01	2.571E+01	1.409E-06	1.946E-07
151111A	3.5	46.34	-7.834E-02	2.810E-01	-1.327E+01	1.421E+05	5.339E+02	2.265E+02	2.239E-06	2.228E-07
151229A	1.4	3.456	-1.307E+00	9.063E-02	-1.042E+01	9.012E+04	2.496E+02	3.396E+01	1.303E-06	6.560E-07
161001A	0.67	2.24	-9.395E-01	8.287E-02	-4.363E+00	2.746E+01	6.223E+02	9.954E+01	1.957E-06	1.054E-06
170113A	1.968	49.15	-1.704E+00	2.232E-01	-2.046E+01	2.384E+10	3.339E+02	1.745E+02	2.861E-06	4.689E-07
171222A	2.409	80.38	-3.713E-01	1.114E+00	-2.135E+00	9.542E-02	5.980E+01	1.410E+01	4.325E-06	4.636E-07
180418A	1.55	2.56	-1.389E+00	9.523E-02	-9.407E+00	5.234E+04	2.680E+03	2.426E+03	9.243E-07	2.409E-07
181010A ^b	1.39	9.728	-6.000E-02	1.430E+00	-1.800E+00	1.700E-01	1.423E+02	9.536E+01	1.260E-06	2.235E-07
190613A ^b	2.78	17.15	-9.190E-01	1.680E-01	-3.013E+00	1.100E+00	4.502E+02	6.124E+01	3.542E-06	2.371E-07
191011A ^b	1.722	25.09	-1.130E+00	5.200E-01	-2.910E+00	1.730E+00	1.502E+02	5.063E+01	1.050E-06	1.645E-07
200829A ^a	1.25	6.912	-4.300E-01	1.000E-02	-2.400E+00	2.000E-02	7.578E+02	9.675E+00	2.891E-04	2.192E-06
201020A ^b	2.903	21.5	-9.400E-01	3.500E-01	-2.470E+00	2.100E-01	1.332E+02	1.975E+01	1.993E-06	1.528E-07
201021C ^b	1.07	35.33	-8.319E-01	3.200E-01	-2.308E+00	6.820E-01	2.575E+02	9.108E+01	2.134E-06	5.552E-07

^a The spectral parameters of 1 GRBs are taken from the GCN.^b The spectral parameters of 5 GRBs are obtained in this work.